Heterostrain-Driven Bandgap Increase in Twisted WS$_2$
A Nanoscale Study

van Heijst, Sabrya E.; Bolhuis, Maarten; Brokkelkamp, Abel; Sangers, Jeroen J.M.; Conesa-Boj, Sonia

Important note
To cite this publication, please use the final published version (if applicable).
Please check the document version above.

Heterostrain-Driven Bandgap Increase in Twisted WS$_2$: A Nanoscale Study

*Sabrya E. van Heijst, Maarten Bolhuis, Abel Brokkelkamp, Jeroen J. M. Sangers, and Sonia Conesa-Boj**

Twisted 2D materials present an enticing platform for exploring diverse electronic properties owning to the tunability of their bandgap energy. However, the intricate relationship between local heterostrain fields, thickness, and bandgap energy remains insufficiently understood, particularly at the nanoscale. Here, it presents a comprehensive nanoscale study elucidating the remarkable sensitivity of the bandgap energy to both thickness and heterostrain fields within twisted WS$_2$ nanostructures. This approach integrates electron energy-loss spectroscopy (EELS) enhanced by machine learning with 4D scanning transmission electron microscopy (STEM). Through this synergistic methodology, enhancements up to 20% in the bandgap energy is unveiled depending on the specimen thickness. This phenomenon is traced back to sizable deformation angles present within individual layers, which can be directly linked to distinct variations in local heterostrain fields. The findings represent a significant advancement in comprehending the electronic behavior of twisted 2D materials and introduce a novel methodological framework with far-reaching implications for twistronics and the investigation of other materials within the nanoscience domain.

1. Introduction

Twisted 2D materials have emerged as promising platforms with tunable electronic properties,[1–6] offering exciting prospects in various fields, including field-effect transistors,[7,8] integrated circuits,[9] and photodetectors.[10,11] A key parameters dictating the electronic behavior of 2D materials is the bandgap energy.[12–21]

S. E. van Heijst, M. Bolhuis, A. Brokkelkamp, J. J. M. Sangers, S. Conesa-Boj
Kavli Institute of Nanoscience
Delft University of Technology
Delft 2628 CJ, The Netherlands
E-mail: s.conesaboj@tudelft.nl

Understanding the influence of factors such as layer count, interlayer distance, twist angle, and local strain fields on the bandgap energy has seen significant progress.[22–26] In particular, the twisted stacking of van der Waals (vdW) materials with Moiré superlattices has emerged as a novel approach to tailor their physical properties by manipulating the crystal symmetry. Recent studies have also highlighted the interplay between extrinsic nonuniform heterostrain and intrinsic atomic reconstruction in the evolution of Moiré structures in twisted 2D materials.[27] This interplay introduces local inhomogeneous intralayer strain within the Moiré, leading to intriguing modulations in the electronic properties.[28–31] Notably, heavily deformed Moirés can exhibit significant modulations in the conduction band, resulting in bandgap variations of up to 300 meV.[32] Additionally, Moiré patterns in hexagonal boron nitride (hBN)-supported monolayer graphene, induced by non-uniform strain fields,[23] have been observed to result in bandgap openings.[24]

Another aspect that deserves attention is the influence of material thickness on bandgap dynamics. Even slight changes in thickness can lead to significant modifications in the bandgap of these unique 2D materials.[12–14,21,33] Thus, achieving a comprehensive understanding of the electronic properties, particularly the dynamics of the bandgap, it is crucial to consider the interplay between material thickness and strain fields.

In this study, we address these challenges by presenting a comprehensive investigation of twisted 2D materials. Specifically, we examine naturally twisted tungsten disulfide (WS$_2$) nanostructures. Two types of nanostructures are considered: i) well-aligned, without Moiré supperlattice, and ii) displaying a spiral-like configuration where each layer is slightly twisted relative to the adjacent ones. Our approach combines electron energy-loss spectroscopy (EELS) enhanced by machine learning techniques[34,35] with 4D scanning transmission electron microscopy (STEM). This multi-pronged methodology enables the accurate evaluation of bandgap energy and local strain fields with nanoscale spatial resolution, facilitating an in-depth exploration of the interplay between bandgap energy, thickness, and strain fields. Our findings reveal a pronounced increase in the bandgap energy within the twisted WS$_2$ specimen characterized by a spiral-like

**ADVANCED
SCIENCE NEWS**

www.advancedsciencenews.com

**ADVANCED
FUNCTIONAL
MATERIALS**

www.afm-journal.de

configuration, by up to 20%, as a function of its local thickness. This phenomenon is traced back to sizable deformation angles present within individual layers, which are accompanied by noticeable changes in local strain fields. This observation highlights the remarkable sensitivity of bandgap dynamics in twisted 2D materials to local strain fluctuations.

Importantly, while our study focuses on van der Waals (vdW) materials, the versatility of our method extends beyond this specific application. It can be easily adapted for strain-field characterization in other low-dimensional nanostructured materials, thereby broadening the spectrum of possible applications.[1–6] Overall, our study offers a comprehensive investigation of the bandgap energy variations in twisted 2D materials, shedding light on the interplay between thickness, strain fields, and electronic properties. The insights gained from this research contribute to the understanding of twistronics and pave the way for future studies exploring the manipulation of local strain for tailored electronic functionalities in various materials.

2. Results and Discussion

2.1. Spatially-Resolved Bandgap and Thickness Correlation Analysis of Twisted WS$_2$

The fabrication process described in the Methods section yields a diverse set of twisted WS$_2$ specimens with varying morphologies. Two distinct twisted structures were inspected using scanning transmission electron microscopy (STEM) imaging, as shown in **Figure 1**a,b. The first specimen (Figure 1a) consists of a large base flake with a smaller flake grown on top and rotated relative to the base flake. The noticeable contrast difference in the STEM image indicates a significant variation in thickness between the base and top flakes. The second specimen (Figure 1b) exhibits a twisted spiral-like structure with multiple layers, each of them slightly twisted compared to the preceding one.

To scrutinise the local electronic properties of these twisted WS$_2$ specimens, we employed spatially-resolved electron energy-loss spectroscopy (EELS) and analyzed the acquired spectral images using the EELSFITTER framework.[34,35] This approach involved parameterizing the dominant zero-loss peak (ZLP) background using deep neural networks,[36] with the Monte Carlo replica method[37] ensuring robust error estimate and propagation. We then subtracted the ZLP pixel by pixel in the spectral image. Subsequently, the bandgap energy and its associated uncertainty were extracted by fitting the onset region of individual subtracted inelastic scattering spectra with a polynomial function.[34] We provide further details of our machine learning methodology in Section S1.1 (Supporting Information).

Figure 1c–f present the spatially-resolved bandgap energy maps and their corresponding relative uncertainties (68% confidence level intervals) for the specimens shown in Figure 1a, b, respectively. The stacked flakes specimen exhibits an indirect bandgap, with the base flake having a bandgap energy ranging from 0.7 to 1.25 eV (Figure 1c) and typical errors varying between 5% and 45% (Figure 1e). The extracted bandgap values in the thicker region associated with the stacked top flake fall towards the lower end of this range, with lower uncertainties compared to the base flake. These bandgap values align with previous reports within the provided uncertainties.[21,33] The bandgap energy in

the twisted flake ranges from 0.6 to 0.8 eV (Figure 1d), with uncertainties predominantly below 50% (Figure 1f), and exhibits a pattern of gradually increasing bandgap values from the outer edges towards the center of the flake. The bandgap type is once again observed to be indirect. The relatively large uncertainties in the bandgap energy reported in Figure 1e,f in a small subset of pixels, for instance close to the edges, reflect the increased level of fluctuations affecting the subtracted inelastic EELS spectra used for the bandgap fitting, as further analyzed in Section S1.1 (Supporting Information).

We further investigate the sensitivity of the bandgap energy to the local thickness for the twisted WS$_2$ specimens of Figure 1a,b by generating the spatially-resolved thickness maps shown in **Figures 2**a,b. These maps are calculated from the EELS spectral images[35] and provide local information on the combined thickness of the specimen and the underlying 5 nm Si$_3$N$_4$ film substrate. The thickness maps for both specimens exhibit negligible uncertainties (at the few-percent level). To characterize the relationship between specimen thickness and bandgap energy, we evaluate the mean bandgap energy values as a function of the corresponding specimen thickness. Figure 2c,d show the result of this evaluation. Within these graphs the red dots represent the weighted average of the mean bandgap values corresponding to a specific thickness range. The 68% confidence level intervals are given in grey and highlight the fluctuations exhibited by the bandgap value at similar thicknesses.

In the stacked flakes specimen (Figure 2c) these latter fluctuations are considerable, indicating a significant variation in the bandgap energy within the specimen. However, when looking at the weighted averages a well-defined trend emerges. This trend indicates a preference for decreasing bandgap energy with increasing thickness, consistent with previous findings reported in the literature.[21,33]

In contrast, the bandgap-thickness correlation analysis of the twisted flake reveals a different trend. Figure 2d indicates that the bandgap energy grows from approximately 0.63 eV to around 0.75 eV as the thickness of the specimen increases. This unexpected trend suggests the presence of other factors influencing the bandgap energy within this twisted flake, beyond the local thickness. The robustness is further supported by the images provided in the Figure S2c,d.

A proposed explanation for this behavior is the presence of local strain fields in the specimen.[17–21,38–40] Motivated by these findings, we further investigated the strain-bandgap relationship by evaluating the corresponding spatially-resolved strain distributions for the same specimens as those for which bandgap energy maps (Figure 1c,d) are obtained.

2.2. Mapping Strain Distributions in Twisted WS$_2$ with 4D STEM-EMPAD

The twisted WS$_2$ specimens investigated in this study exhibit a specific type of strain known as heterostrain. Heterostrain arises when adjacent 2D layers have unequal in-plane strains. This type of strain is particularly relevant in the context of stacking van der Waals (vdW) materials, which are the focus of our investigation. A key challenge in this field is to find a non-invasive method to quantitatively quantify strain in vdW materials.
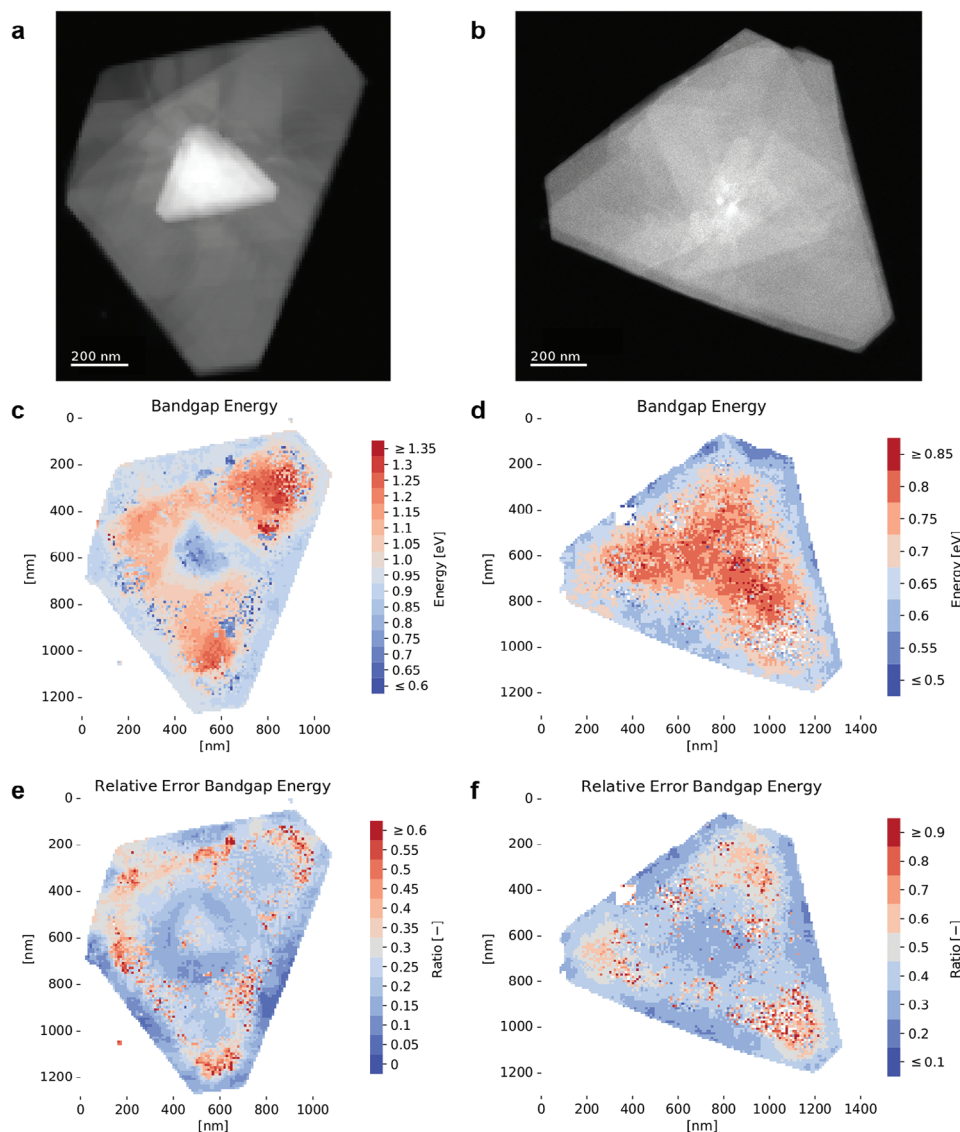
**ADVANCED
SCIENCE NEWS**

www.advancedsciencenews.com

**ADVANCED
FUNCTIONAL
MATERIALS**

www.afm-journal.de

Figure 1. Spatially-resolved bandgap of twisted WS$_2$ specimens. a,b) Low-magnification STEM images of (a) a WS$_2$ specimen consisting of a stack of two rotated flakes, and (b) a twisted WS$_2$ flake. c,d) Spatially-resolved bandgap energy maps corresponding to the specimens in (a) and (b), respectively. e,f) The relative uncertainties (68% confidence level intervals) associated to the bandgap energy maps. In (c–f) a mask has been applied to exclude substrate-only pixels and specimen pixels with a relative uncertainty exceeding 100%.

While conventional techniques based on transmission electron microscopy (TEM), such as geometrical phase analysis (GPA),[41] have been employed to analyze strain in 2D materials,[42] they are limited by the requirement of atomic-resolution imaging, which restricts the field-of-view to a few tens of nanometers. Consequently, deploying such methods for evaluating strain fields across an entire micron-sized nanostructure is highly challenging.

To overcome this limitation, we leverage the capabilities of 4D scanning transmission electron microscopy (STEM) coupled with an Electron Microscopy Pixel Array Detector (EMPAD).[43] The utilization of the EMPAD detector plays a crucial role in our approach, as it enables the acquisition of images that facilitate the comprehensive extraction of strain information across

the entire specimen. By employing STEM in scanning nanobeam diffraction mode, we can capture nanobeam diffraction maps at each real-space scan position. This results in a comprehensive 4D dataset where the spatial variations in strain are revealed throughout the specimen. By analyzing this 4D dataset, we gain a deeper understanding of the strain characteristics within the WS$_2$ specimens and their implications for the bandgap properties.

In this work, we utilized the recently developed STRAINMAP-PER open-source framework, which significantly enhances the capabilities of an existing approaches to strain analyses based on 4D-STEM.[44] By incorporating advanced features such as the tracking of inter-atomic spacing peaks and the integration of clustering within the analysis framework, STRAINMAPPER enables the extraction of local intra-layer strain and rigid rotation
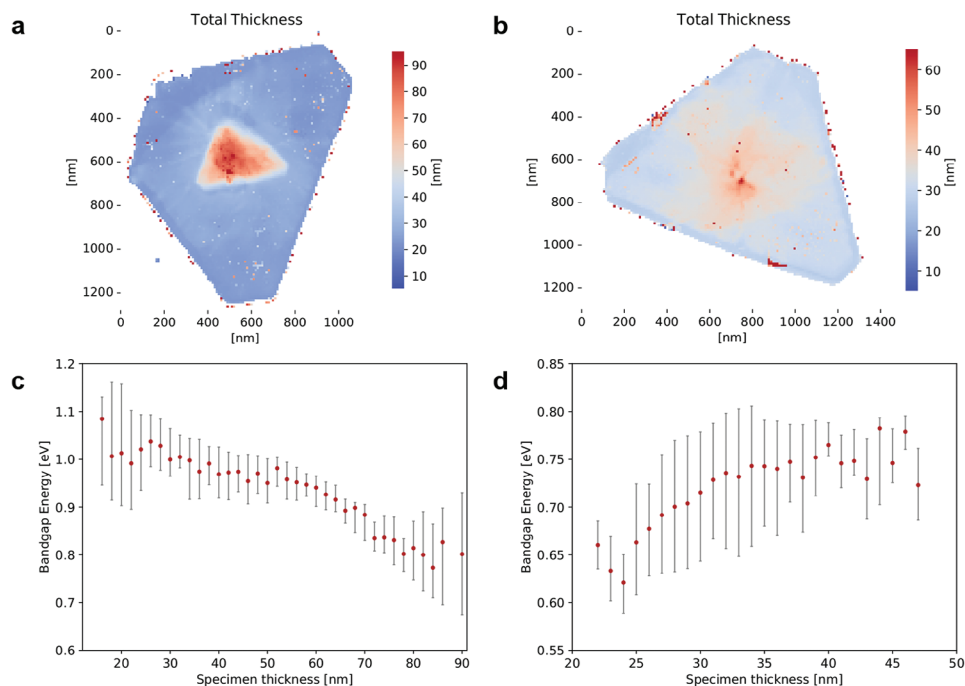
**ADVANCED
SCIENCE NEWS**

www.advancedsciencenews.com

**ADVANCED
FUNCTIONAL
MATERIALS**

www.afm-journal.de

Figure 2. Thickness dependence of the bandgap energy in twisted WS_2 specimens. a,b) Spatially-resolved local thickness maps of the specimens depicted in Figure 1a,b, respectively. These maps include the contribution from the underlying 5 nm Si_3N_4 film substrate. A mask has been applied to exclude substrate-only pixels and specimen pixels with a relative uncertainty exceeding 100%. c,d) Correlation between specimen thickness and bandgap energy where the data is divided, with regard to the thickness, into bins of (c) 2 nm and (d) 1 nm in size. The red dots represent the weighted averages of the bandgap energy per thickness bin, with 68% confidence level intervals given in grey.

(or deformation) angles θ from 4D nanobeam diffraction datasets. Our calculation captures the local deformations within a layer that are induced by the inter-layer orientations, thereby expanding its applicability to a wider range of specimens. One should emphasise here that this rigid rotation (deformation) angle that is discussed in the following does not coincide in general with a global twist angle between adjacent layers, see Section S2.2 (Supporting Information) for an extended discussion of their relationship.

2.2.1. WS₂ Stacked Flakes

For the analysis of the stacked flakes specimen, the corresponding annular dark-field scanning transmission electron microscopy (ADF-STEM) image of the scanned area is presented in **Figure 3**a. Since we are inspecting large (micrometer-sized) specimens with nanoscale resolution, in general not all regions will be on axis (with the electron beam aligned with a main crystallographic axis), a core requirement for most strain characterization methods. To recover the information hidden in the regions of the specimen in low-symmetry view, we extend 4D-STEM by means of the exit-wave power cepstrum (EWPC) approach[44] based on the conversion of nanobeam diffraction maps. This procedure results into an auto-correlation of the real lattice which also contains peaks corresponding to inter-atomic spacings, see Section S2.1 (Supporting Information) for more details. By comparing these EWPC patterns across the full specimen, one can determine the required in-

formation about inter-plane distances to evaluate local strain fields.

Figure 3b illustrates one such EWPC pattern, corresponding to a nanobeam diffraction map acquired at a pixel where the second flake is stacked on the base flake (indicated by the red dot in Figure 3a). The observed hexagonal pattern reflects the characteristic honeycomb lattice structure of WS_2. For improved clarity, we display the EWPC pattern on a capped linear scale instead of the usual logarithmic scale (see Figure S5b, Supporting Information). This adjustment enhances the visibility of key features within the pattern, specifically the inter-atomic spacing peaks.

The detected peaks in the EWPC pattern consistently appear across the entire scanned area and provide a reliable representation of the underlying structural information. By tracking and superimposing these peaks within each pattern, we generate the weighted point cloud shown in Figure 3c, where each spot corresponds to a unique peak location and whose color indicates the peak detection frequency. A threshold filter is applied to remove low-frequency spots ($\leqslant 50$). These spots often correspond to erroneously tracked peaks, such as those within the substrate region (see Figures S5d,f, Supporting Information). Refer to Figure S5c (Supporting Information) for the pre-filtered counterpart. The spots in Figure 3c are categorized into 12 clusters based on their position and weight, with each cluster grouping together the corresponding peak positions from different EWPC patterns representing the same feature. Of these 12 clusters, six of them display a much higher population.

The information provided by these tracked peak positions can be used to determine spatially-resolved strain and rigid
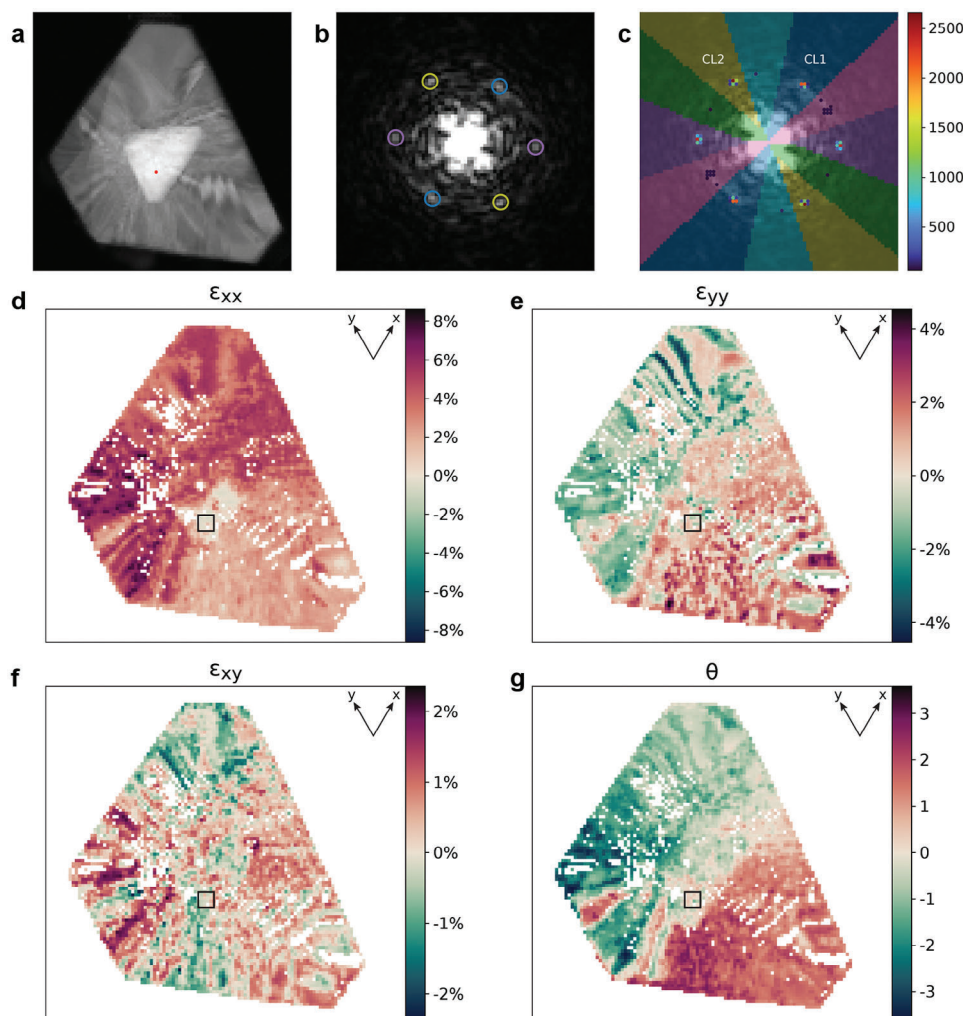
**ADVANCED
SCIENCE NEWS**

www.advancedsciencenews.com

**ADVANCED
FUNCTIONAL
MATERIALS**

www.afm-journal.de

Figure 3. Spatially-resolved determination of strain fields and deformation angles from 4D STEM-EMPAD measurements in a WS_2 stacked specimen. a) ADF-STEM image of the stacked flakes specimen shown in Figure 1a as obtained from the 4D STEM-EMPAD dataset. b) EWPC pattern extracted at the red pixel in (a). A capped linear scale is used to enhance the visualization of the inter-atomic spacing peaks. c) Weighted point cloud displaying all uniquely tracked peak locations (spots) along with their corresponding weights (color). A threshold was applied to remove all spots found 50 times or less. Colored divisions represent clustering of the point cloud. Spatially-resolved (d,f) strain maps and (g) rotation map of the specimen obtained using the marked clusters in (c). The strain maps correspond to the ϵ_{xx}, ϵ_{yy}, and ϵ_{xy} components, respectively. The reference area is indicated by the black square. The maps were subjected to a Gaussian filter to smooth out outliers.

rotation (deformation) angle maps across the whole specimen as follows. First, one chooses a reference region, which specifies the baseline for the evaluation of the (relative) strain fields and rigid rotation angles. Then, we select two non-parallel clusters that belong to the same set of peaks within the EWPC pattern, such that the chosen clusters provide information about a given structural element. In the case of WS_2, a single crystal imaged on-axis would lead to the characteristic hexagonal pattern composed by six peaks, while two WS_2 crystals, one rotated with respect to the other, would result in 12 peaks. Here, the chosen structural element is the dominant set of six peaks organized in a hexagonal pattern corresponding to the same crystal. The vectors associated with the peak positions in the chosen clusters, labeled as CL1 and CL2 in Figure 3c, form the basis for the resulting strain and rotation angle characterization.

The corresponding results of the spatially-resolved strain and rotation analysis for the stacked flakes specimen are presented in Figure 3d–g, with the chosen reference area indicated by the black square. The strain maps were decomposed into components along the x- and y-directions, as well as the xy component (shear strain). In order to enhance visualization and mitigate pixelation artifacts and outliers, a Gaussian filter was applied to smoothen the maps, with the original maps depicted in Figure S7 (Supporting Information) for completeness. In some instances within the strain and rotation maps, empty pixels can be observed at specific real-space scan positions, indicating that one of the two chosen peaks could not be tracked or was not tracked correctly at those particular positions.

From the maps in Figure 3d,f, it is observed that strain is present throughout the entire specimen. However, no distinct divisions into specific strain areas can be discerned. On average,
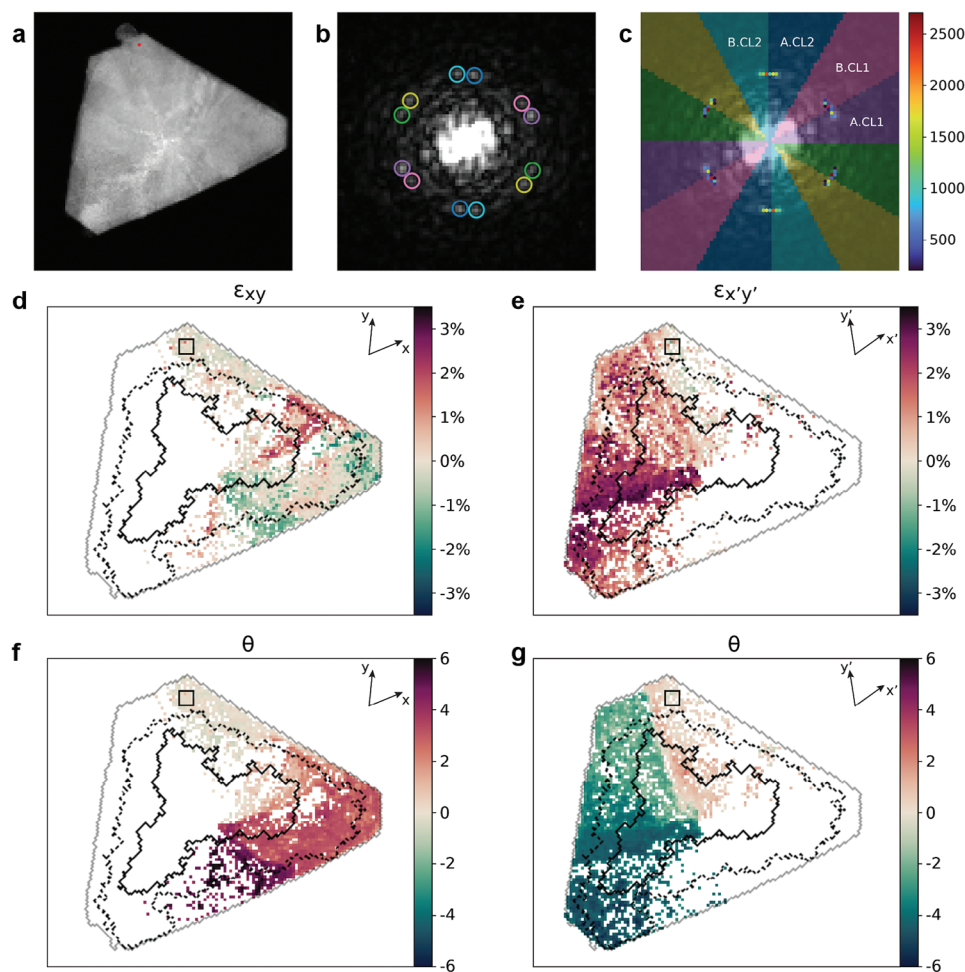
Figure 4. Spatially-resolved determination of strain field and deformation angles from 4D STEM-EMPAD measurements in a twisted WS_2 flake. a) ADF-STEM image of the twisted flake from Figure 1b obtained from the 4D STEM-EMPAD dataset. b) EWPC pattern extracted at the red pixel in (a). A capped linear scale is used to enhance the visualization of the inter-atomic spacing peaks. c) Weighted point cloud displaying all uniquely tracked peak locations (spots) along with their corresponding weights (color). Substrate pixels were excluded from the peak tracking using a mask based on the ADF image contrast. Additionally, a threshold was applied after peak tracking to remove all spots found 200 times or less. Colored divisions represent clustering of the point cloud. Spatially-resolved (d,e) strain (ϵ_{xy}) maps and (f,g) rotation maps of the specimen obtained using the marked clusters in (c) denoted by (d,f) A and (e,g) B. The reference area is indicated by the black square. The maps were subjected to a Gaussian filter to smooth out the outliers. The overlaid lines outline the contours of the bandgap map of Figure 1d, specifically, the crossings at 0.7 eV (dashed black line) and 0.8 eV (solid black line). The outline of the entire flake is represented by the solid grey line.

it can be concluded that the strain exhibits a relatively uniform distribution across the entire specimen. This uniformity is even more apparent when focusing specifically on the shear strain component (ϵ_{xy}), as illustrated in Figure 3f. The relative shear strain values predominantly fall within the approximate range of ± 1.1%.

To gain further insights into these observations, a high-angle annular dark-field (HAADF) STEM analysis is conducted, as illustrated in Figure S10a-c (Supporting Information). This analysis confirms that the specimen possesses a pristine crystal structure. In the case of the stacked flakes specimen, as previously mentioned, the trend observed in the bandgap energy in relation to the specimen thickness (Figure 2c) aligns with previous reports in the literature.[21,33] In these reported pristine specimens, thickness serves as the primary factor influencing bandgap modification, in agreement with our findings.

2.2.2. Twisted WS_2 Flake

The same local strain field characterization was carried out on the naturally twisted flake shown in Figure 1b. The ADF-STEM image of the scanned area for this analysis, extracted from the 4D dataset, is depicted in **Figure 4**a. The nanobeam diffraction map obtained at the red dot in Figure 4a was transformed into the EWPC pattern shown in Figure 4b. Twelve peaks were identified within this specific pattern. Prior to peak-tracking, the data was masked using the contrast in the ADF image to exclude substrate pixels. As in Figure 3c, a threshold filter is applied to remove low-frequency (≤200) spots resulting from any remaining erroneously tracked peaks. The filtered weighted point cloud obtained by tracking the 12 peaks across the specimen is depicted in Figure 4c.

**ADVANCED
SCIENCE NEWS**

www.advancedsciencenews.com

**ADVANCED
FUNCTIONAL
MATERIALS**

www.afm-journal.de

Unlike the stacked flakes specimen, the clustering of the weighted point cloud of the twisted flake specimen exhibited clear divisions. A total of 12 distinct clusters were identified, which are visually represented by the colored divisions. Six of these clusters correspond to one region of the flake and the remaining six to the complementary region. This division into two distinct regions demands the analysis of the twisted flake specimen to be split. These two regions (denoted by A and B) overlap in a small area, including the pixel selected in Figures 4a, which provides a natural choice to define the reference for the strain analysis.

Similar to the analysis conducted for the stacked flakes specimen, for strain and rotation calculations we considered two non-parallel clusters, denoted by A.CL1, A.CL2, and B.CL1, B.CL2 in Figure 4c for the two regions A and B, respectively. The selected clusters belong to the same set of peaks within the EWPC pattern, ensuring that they provide information about the same structural elements, and each of them represents a complementary region of the specimen. The reference area for strain calculation, indicated by a black square, was as mentioned above chosen to encompass the region that displays all twelve spots in the EWPC pattern.

The spatially-resolved shear strain (ϵ_{xy}) and rotation maps obtained from cluster set A, corresponding to vectors along the x and y directions, are presented in Figure 4d,f. The shear strain and rotation maps obtained from cluster set B, corresponding to vectors along the x' and y' directions, are presented in Figure 4e,g. The additional strain components (ϵ_{xx}, ϵ_{yy}, $\epsilon_{x'x'}$, $\epsilon_{y'y'}$) are provided in Figure S6 (Supporting Information). Similar to the stacked flakes specimen, these maps were subjected to a Gaussian filter for enhanced visualization, with the original maps provided in Figures S8 and S9 (Supporting Information).

The analysis of Figure 4d,e reveals that the strain distribution in this twisted flake is not uniform, in contrast to the stacked flakes specimen. Regions of both tensile strain, reaching up to 3%, and compressive strain, down to −1.5%, are observed relative to the chosen reference. Notably, abrupt changes in the strain field are found at specific locations, particularly near the three corners of the flake. For example, at the top of the flake, there is a sudden transition to a tensile strain of approximately 1.5% relative to the near-zero strain of the reference region to its right. A similar transition is observed in the right corners, whereas the left corner exhibits a change between low (1.5%) and high (3%) tensile strain values.

Regarding the deformation angles of this twisted flake, a similar distribution with abrupt transitions is observed, as shown in Figure 4f,g. The deformation angles θ determined across the twisted flake specimen exhibit a comparable pattern, characterized by abrupt changes near the three corners of the flake. At the top of the flake, there is a transition to approximately −2° relative to the near-zero rotation angle in the reference area. In the right corner, a transition in the opposite rotational direction occurs toward approximately 3°. Similarly, at the left corner, there is a transition between low (around −2°) and high (around −5°) rotation angle values. Overall, these deformation angles mostly fall within the range of ±5°. These results are consistent with previous findings, particularly regarding the non-uniform distribution of strain across bilayer structures and the significant influence of

changes in relative rotation angles between layers on these strain fields.[22]

It is worth mentioning here that our methodology to quantify strain and rigid rotation angles is also suitable to analyse van der Waals heterostructures characterized by a large twist global rotation angle, as demonstrated with the twisted bilayer $MoSe_2$/WSe_2 heterostructure reported in Section S4 (Supporting Information).

2.3. Correlation between Bandgap Energy and Strain Distribution in Twisted WS_2 Flake

To obtain a better understanding of the relationship between bandgap energy and strain distribution in the twisted WS_2 specimen, we generated an approximate outline of the constant-energy contours from the bandgap map (Figure 1d) and overlaid it onto the spatially-resolved maps presented in Figure 4d,g. Specifically, the overlay highlights the crossings of the bandgap energy at values of 0.7 eV (dashed black line) and 0.8 eV (solid black line). The outline of the entire flake (solid grey line) is included for reference. This illustrative approach effectively highlights the correlation between the regions experiencing sudden variations in the strain and rotation maps, and areas where the bandgap is enhanced. This observation establishes a distinct correlation between the specimen's non-uniform strain distribution and the associated alterations in the bandgap.

Analogous to the stacked flakes specimen, the twisted flake was subjected to a HAADF-STEM analysis presented in Figure S10d,f (Supporting Information). The analysis of the STEM images provided valuable insights into the crystal structure of the twisted flake. Contrary to pristine ordered planes, the images revealed the presence of Moiré patterns across multiple regions of the specimen. These patterns signify a deviation from conventional crystal characteristics, suggesting the potential for unconventional behavior within the material.

The detailed analysis of Figure 4, together with the bandgap-thickness correlation illustrated in Figure 2d, provides compelling evidence establishing the relationship between the local strain field and the bandgap energy in twisted WS_2 flakes. Our results suggest that regions within the specimen, exhibiting varying local strain fields due to the presence of twisted adjacent layers, demonstrate an enhancement in bandgap energy. This enhancement becomes apparent when compared to a reference specimen of similar thickness but devoid of significant strain field variations. This observed trend is consistent with predicted effects of strain on bandgap energy, where a change of approximately 100 meV per percent of applied strain is anticipated. Further, variations in interlayer coupling due to twist angles and layer separations, as revealed by DFT calculations,[45] provide additional support for the reported interplay between strain and bandgap modification.

3. Summary and Outlook

In this extensive study, we have fingerprinted the interdependent local electronic properties, thickness, and strain fields in twisted and stacked WS_2 flakes, focusing on their cross-correlations, by means of advanced imaging techniques and computational analysis methods.

**ADVANCED
SCIENCE NEWS**

www.advancedsciencenews.com

**ADVANCED
FUNCTIONAL
MATERIALS**

www.afm-journal.de

In the case of the stacked flakes specimen, we observed a uniform strain distribution across the entire specimen, with particular emphasis on the shear strain component. This uniformity suggests the preservation of the pristine crystal structure, enabling bandgap energy modification primarily driven by local thickness variations. Our findings align with the well-established understanding of the relationship between thickness and bandgap modifications in 2D materials.

In stark contrast, the twisted flake displayed a non-uniform strain distribution, featuring localized regions of enhanced strain and abrupt variations. These strain variations were accompanied by enhancements in the bandgap energy, dominating over the conventional bandgap-thickness correlation. Notably, the bandgap energy in the twisted flake increased by up to 20%, highlighting the profound influence of the deformation angle on the electronic properties. This unexpected behavior challenges conventional expectations and underscores the vast potential of strain engineering in the emerging field of twistronics.

Furthermore, the presence of Moiré patterns in the twisted flake further emphasized the deviation from the pristine crystal structure. These patterns, arising from lattice mismatch and rotational misalignment, introduced additional complexities and contributed to the observed unconventional behavior. The complex interplay between strain variations and Moiré patterns presents a promising avenue for exploring novel physical phenomena and designing advanced electronic devices.

Our findings highlight the significance of non-uniform strain distribution and the role of deformation angle in modulating the bandgap energy of 2D materials. The ability to precisely control strain fields in twisted flakes opens up exciting opportunities for engineering their electronic and optical properties. This contribution adds to the growing field of twistronics, offering valuable insights into the intricate relationship between strain, bandgap energy, and unconventional behavior in 2D materials.

4. Experimental Section

Fabrications of Naturally Twisted WS$_2$ Specimens: The twisted WS$_2$ specimens were grown directly on a TEM microchip. This microchip consisted of a silicon frame with nine windows, each spanned by a 5 nm thick Si$_3$N$_4$ film. Tungsten trioxide (WO$_3$) powder, which acts as a seeding material, was deposited on this microchip. This was achieved by dispersing 50 mg of WO$_3$ in 1 mL of isopropanol and then depositing a few drops of this solution onto the substrate using a pipette. After the sample was left to dry, the WO$_3$ had been successfully spread over the TEM microchip. Following this preparation, the WO$_3$ coated TEM microchip was placed in the central heating zone of a gradient tube furnace from Carbolite Gero. A crucible containing sulfur powder was positioned in a separate heating zone upstream. The central heating zone was heated to a temperature of 750 °C, followed by heating the zone containing the sulfur powder to 220 °C. The system was maintained at these temperatures for one hour under a consistent argon flow of 150 sccm. Before this process, the system was flushed using an argon flow of 500 sccm for 30 min. Once the reaction time had passed, the furnace was cooled down naturally.

STEM-EELS Measurement Details: The STEM-EELS measurements were performed on an ARM200F Mono-JEOL microscope. The microscope was operated at 200 kV with the monochromator ON and a slit of 1.3 μm inserted. A Gatan GIF Quantum ERS system (model 966) was used for the EELS analyses. The convergence and collection semi-angles were 19.96 and 14.5 mrad, respectively. EEL spectra were acquired with an entrance aperture diameter of 5 mm, energy dispersion of 0.015 eV/channel, and pixel time of 0.5 s. For the EELS analyses and STEM imaging of Figure 1a,b a camera length of 12 cm was used. Following acquisition, the data were analyzed using the open-source analysis framework EELSFITTER, yielding the maps shown in Figures 1c–f and 2a,b and Figures S1 and S2 (Supporting Information).

4D STEM Experimental Acquisition Details: The 4D STEM measurements were conducted on a Titan Cube microscope equipped with an EMPAD detector. The microscope was operated at 300 kV in STEM nanoprobe mode. For the twisted WS$_2$ specimens, the convergence semi-angle was reduced to 2.63 mrad using a 50 m condenser (C2) aperture and a camera length of 285 mm. Acquisitions were carried out at 1 ms exposure time for 128 × 128 real-space pixels (scan positions). For each of these pixels, the EMPAD detector records a nanobeam diffraction pattern of 128 x 128 pixels. Similarly, for the twisted MoSe$_2$/WSe$_2$ heterostructure, the convergence semi-angle was reduced to 0.53 mrad using a 10 m condenser (C2) aperture and a camera length of 285 mm. Acquisitions were carried out at 5 ms exposure time. Analysis of the datasets was performed using the recently developed STRAINMAPPER framework, producing the results reported in Figures 3 and 4 and Figures S3 and S5 (Supporting Information) through Figures S9 and S12 (Supporting Information).

High-Resolution STEM Image Acquisition Details: The high-resolution STEM images in Figure S10 (Supporting Information) were collected on an ARM200F Mono-JEOL microscope operated at 200 kV. The convergence semi-angle and camera length were 19.82 mrad and 8 cm, respectively. The high-resolution STEM images for Figure S11b,c (Supporting Information) were collected on a Titan Cube microscope operated at 300 kV.

Supporting Information

Supporting Information is available from the Wiley Online Library or from the author.

Author Contributions

S.E.v.H. synthesized the analyzed specimens. S.E.v.H. conducted experiments and collected data. M.B. worked on the code and the user interface for the strain mapping. A.B. worked on the code and the user interface for the EELS analysis. M.B., S.E.v.H., J.J.M.S., and A.B. conducted data analysis and interpretation, with input from S.C-B., S.E.v.H., and S.C.-B. were responsible for writing the initial draft of the manuscript, with input and revisions from all authors. S.C.-B., M.B., S.E.v.H., and A.B. all contributed to reviewing and editing the manuscript. All authors have read and approved the final version of the manuscript. S.C.-B supervised all aspects of the project.

Conflict of Interest

The authors declare no conflict of interest.

Data Availability Statement

The data that support the findings of this study are available from the corresponding author upon reasonable request.

[1] Y. Shimazaki, I. Schwartz, K. Watanabe, T. Taniguchi, M. Kroner, A. Imamoğlu, *Nature* **2020**, *580*, 472.

[2] W. Yan, L. Meng, Z. Meng, Y. Weng, L. Kang, X.-a. Li, *J. Phys. Chem. C* **2019**, *123*, 30684.

[3] F. Wu, T. Lovorn, E. Tutuc, I. Martin, A. H. MacDonald, *Phys. Rev. Lett.* **2019**, *122*, 086402.

[4] K. Tran, G. Moody, F. Wu, X. Lu, J. Choi, K. Kim, A. Rai, D. A. Sanchez, J. Quan, A. Singh, J. Embley, A. Zepeda, M. Campbell, T. Autry, T. Taniguchi, K. Watanabe, N. Lu, S. K. Banerjee, K. L. Silverman, S. Kim, E. Tutuc, L. Yang, A. H. MacDonald, X. Li, *Nature* **2019**, *567*, 71.

[5] Y. Cao, V. Fatemi, S. Fang, K. Watanabe, T. Taniguchi, E. Kaxiras, P. Jarillo-Herrero, *Nature* **2018**, *556*, 43.

[6] C. R. Dean, L. Wang, P. Maher, C. Forsythe, F. Ghahari, Y. Gao, J. Katoch, M. Ishigami, P. Moon, M. Koshino, T. Taniguchi, K. Watanabe, K. L. Shepard, J. Hone, P. Kim, *Nature* **2013**, *497*, 598.

[7] H. Wang, L. Yu, Y.-H. Lee, Y. Shi, A. Hsu, M. L. Chin, L.-J. Li, M. Dubey, J. Kong, T. Palacios, *Nano Lett.* **2012**, *12*, 4674.

[8] B. Radisavljevic, A. Radenovic, J. Brivio, V. Giacometti, A. Kis, *Nat. Nanotechnol.* **2011**, *6*, 147.

[9] B. Radisavljevic, M. B. Whitwick, A. Kis, *ACS Nano* **2011**, *5*, 9934.

[10] S. R. Tamalampudi, Y.-Y. Lu, R. U. Kumar, R. Sankar, C.-D. Liao, K. B. Moorthy, C.-H. Cheng, F. C. Chou, Y.-T. Chen, *Nano Lett.* **2014**, *14*, 2800.

[11] L. Ye, H. Li, Z. Chen, J. Xu, *ACS Photonics* **2016**, *3*, 692.

[12] G. Zhang, S. Huang, A. Chaves, C. Song, V. O. Özçelik, T. Low, H. Yan, *Nat. Commun.* **2017**, *8*, 14071.

[13] L. Li, J. Kim, C. Jin, G. J. Ye, D. Y. Qiu, F. H. da Jornada, Z. Shi, L. Chen, Z. Zhang, F. Yang, K. Watanabe, T. Taniguchi, W. Ren, S. G. Louie, X. H. Chen, Y. Zhang, F. Wang, *Nat. Nanotechnol.* **2017**, *12*, 21.

[14] T. Li, G. Galli, *J. Phys. Chem. C* **2007**, *111*, 16192.

[15] S. Zheng, L. Sun, X. Zhou, F. Liu, Z. Liu, Z. Shen, H. J. Fan, *Adv. Opt. Mater.* **2015**, *3*, 1600.

[16] K. Liu, L. Zhang, T. Cao, C. Jin, D. Qiu, Q. Zhou, A. Zettl, P. Yang, S. G. Louie, F. Wang, *Nat. Commun.* **2014**, *5*, 4966.

[17] J. Quereda, P. San-Jose, V. Parente, L. Vaquero-Garzon, A. J. Molina-Mendoza, N. Agraït, G. Rubio-Bollinger, F. Guinea, R. Roldán, A. Castellanos-Gomez, *Nano Lett.* **2016**, *16*, 2931.

[18] Y. Li, T. Wang, M. Wu, T. Cao, Y. Chen, R. Sankar, R. K. Ulaganathan, F. Chou, C. Wetzel, C.-Y. Xu, *2D Mater.* **2018**, *5*, 021002.

[19] A. Castellanos-Gomez, R. Roldán, E. Cappelluti, M. Buscema, F. Guinea, H. S. J. van der Zant, G. A. Steele, *Nano Lett.* **2013**, *13*, 5361.

[20] H. J. Conley, B. Wang, J. I. Ziegler, R. F. Haglund Jr, S. T. Pantelides, K. I. Bolotin, *Nano Lett.* **2013**, *13*, 3626.

[21] W. S. Yun, S. W. Han, S. C. Hong, I. G. Kim, J. D. Lee, *Phys. Rev. B* **2012**, *85*, 033305.

[22] H. Kumar, D. Er, L. Dong, J. Li, V. B. Shenoy, *Sci. Rep.* **2015**, *5*, 10872.

[23] C. R. Woods, L. Britnell, A. Eckmann, R. S. Ma, J. C. Lu, H. M. Guo, X. Lin, G. L. Yu, Y. Cao, R. V. Gorbachev, A. V. Kretinin, J. Park, L. A. Ponomarenko, M. I. Katsnelson, Yu. N. Gornostyrev, K. Watanabe, T. Taniguchi, C. Casiraghi, H.-J. Gao, A. K. Geim, K. S. Novoselov, *Nat. Phys.* **2014**, *10*, 451.

[24] S. Tang, H. Wang, Y. Zhang, A. Li, H. Xie, X. Liu, L. Liu, T. Li, F. Huang, X. Xie, M. Jiang, *Sci. Rep.* **2013**, *3*, 2666.

[25] K. Roy, M. Padmanabhan, S. Goswami, T. P. Sai, G. Ramalingam, S. Raghavan, A. Ghosh, *Nat. Nanotechnol.* **2013**, *8*, 826.

[26] H. Fang, C. Battaglia, C. Carraro, S. Nemsak, B. Ozdol, J. S. Kang, H. A. Bechtel, S. B. Desai, F. Kronast, A. A. Unal, G. Conti, C. Conlon, G. K. Palsson, M. C. Martin, A. M. Minor, C. S. Fadley, E. Yablonovitch, R. Maboudian, A. Javey, *Proc. Natl. Acad. Sci. USA* **2014**, *111*, 6198.

[27] P. Ci, Y. Zhao, M. Sun, Y. Rho, Y. Chen, C. P. Grigoropoulos, S. Jin, X. Li, J. Wu, *Nano Lett.* **2022**, *22*, 9027.

[28] N. C. H. Hesp, I. Torre, D. Rodan-Legrain, P. Novelli, Y. Cao, S. Carr, S. Fang, P. Stepanov, D. Barcons-Ruiz, H. H. Sheinfux, K. Watanabe, T. Taniguchi, D. K. Efetov, E. Kaxiras, P. Jarillo-Herrero, M. Polini, F. H. L. Koppens, *Nat. Phys.* **2021**, *17*, 1162.

[29] Y. Jiang, X. Lai, K. Watanabe, T. Taniguchi, K. Haule, J. Mao, E. Y. Andrei, *Nature* **2019**, *573*, 91.

[30] L. Huder, A. Artaud, T. L. Quang, G. T. de Laissardiére, A. G. M. Jansen, G. Lapertot, C. Chapelier, V. T. Renard, *Phys. Rev. Lett.* **2018**, *120*, 156405.

[31] C. Zhang, M.-Y. Li, J. Tersoff, Y. Han, Y. Su, L.-J. Li, D. A. Muller, C.-K. Shih, *Nat. Nanotechnol.* **2018**, *13*, 152.

[32] K. Li, F. Xiao, W. Guan, Y. Xiao, C. Xu, J. Zhang, C. Lin, D. Li, Q. Tong, S.-Y. Li, A. Pan, *Nano Lett.* **2022**, *22*, 5997.

[33] A. Kuc, N. Zibouche, T. Heine, *Phys. Rev. B* **2011**, *83*, 245213.

[34] L. I. Roest, S. E. van Heijst, L. Maduro, J. Rojo, S. Conesa-Boj, *Ultramicroscopy* **2021**, *222*, 113202.

[35] A. Brokkelkamp, J. ter Hoeve, I. Postmes, S. E. van Heijst, L. Maduro, A. V. Davydov, S. Krylyuk, J. Rojo, S. Conesa-Boj, *J. Phys. Chem. A* **2022**, *126*, 1255.

[36] R. D. Ball, S. Carrazza, J. Cruz-Martinez, L. Del Debbio, S. Forte, T. Giani1, S. Iranipour, Z. Kassabov, J. I. Latorre, E. R. Nocera, R. L. Pearson1, J. Rojo, R. Stegeman, C. Schwan, M. Ubiali, C. Voisey, M. Wilson1, *Eur. Phys. J. C* **2022**, *82*, 428.

[37] A. Candido, A. Garcia, G. Magni, T. Rabemananjara, J. Rojo, R. Stegeman, *JHEP* **2023**, *05*, 149.

[38] S. H. Sung, N. Schnitzer, L. Brown, J. Park, R. Hovden, *Phys. Rev. Mater.* **2019**, *3*, 064003.

[39] F. Miao, S.-J., Liang, B. Cheng, *npj Quantum Mater.* **2021**, *6*, 59.

[40] S. Zhu, H. T. Johnson, *Nanoscale* **2018**, *10*, 20689.

[41] J. Rouvière, E. Sarigiannidou, *Ultramicroscopy* **2005**, *106*, 1.

[42] M. Tinoco, L. Maduro, M. Masaki, E. Okunishi, S. Conesa-Boj, *Nano Lett.* **2017**, *17*, 7021.

[43] M. C. Cao, Y. Han, Z. Chen, Y. Jiang, K. X. Nguyen, E. Turgut, G. D. Fuchs, D. A. Muller, *Microscopy* **2017**, *67*, i150.

[44] E. Padgett, M. E. Holtz, P. Cueva, Y.-T. Shao, E. Langenberg, D. G. Schlom, D. A. Muller, *Ultramicroscopy* **2020**, *214*, 112994.

[45] P. Johari, V. B. Shenoy, *ACS Nano* **2012**, *6*, 5449.